Geostationary interferometric SAR: orbit design and control implementation

Matteo Monti[1], Andrea Monti Guarnieri[1], Francesca Pelliccia[1], and Alfredo Renga[1]

[1]Affiliation not available

January 20, 2025

Abstract

The Geostationary Synthetic Aperture Radar (GEO SAR) concept aims at defining an Earth Observation system able to provide regional coverage with large swaths and subcontinental access with a very short revisit time by exploiting the unique characteristics of the GEO orbit. These peculiar characteristics make GEO SAR suitable for imaging and interferometry of fastevolving large-scale phenomena, such as ground motion or water vapor. The design of the orbit for a GEO SAR is discussed to provide, at one time, wide imaging capability, compensation for the huge power loss due to the distance, and short interferometric revisit. In particular, interferometry imposes constraints on the repeatability of the orbit that are far more restrictive than the control required for telecommunication satellites. Here, two different specific control approaches are proposed to ensure small normal baselines and to maximize angular band overlap between subsequent acquisitions. The first one is based on four control maneuvers per orbit period that exploits tangential, normal, and radial burns, whereas the second one reduces to three the required daily maneuvers that are performed only in tangential and normal directions. The latter assures accurate motion repetition while saving the required ΔV .

Geostationary interferometric SAR: orbit design and control implementation

Matteo Monti, Andrea Monti Guarnieri, Francesca Pelliccia, Alfredo Renga

***Abstract*—The Geostationary Synthetic Aperture Radar (GEO SAR) concept aims at defining an Earth Observation system able to provide regional coverage with large swaths and subcontinental access with a very short revisit time by exploiting the unique characteristics of the GEO orbit. These peculiar characteristics make GEO SAR suitable for imaging and interferometry of fast-evolving large-scale phenomena, such as ground motion or water vapor.**

The design of the orbit for a GEO SAR is discussed to provide, at one time, wide imaging capability, compensation for the huge power loss due to the distance, and short interferometric revisit. In particular, interferometry imposes constraints on the repeatability of the orbit that are far more restrictive than the control required for telecommunication satellites. Here, two different specific control approaches are proposed to ensure small normal baselines and to maximize angular band overlap between subsequent acquisitions. The first one is based on four control maneuvers per orbit period that exploits tangential, normal, and radial burns, whereas the second one reduces to three the required daily maneuvers that are performed only in tangential and normal directions. The latter assures accurate motion repetition while saving the required ΔV.

***Index Terms*—Radar imaging, Synthetic Aperture Radar (SAR), Earth Observing System, radar interferometry, geosynchronous SAR, geostationary SAR, orbit control, station-keeping**

I. Introduction

SYNTHETIC Aperture Radar (SAR) is an active microwave imaging sensor mounted on a moving platform (airborne or spaceborne) that can be used to obtain high-resolution images by synthesizing a huge antenna, as the combination of multiple along-track observations [1], [2]. The peculiarity of these systems is that thanks to microwave signals, they can operate day or night, through clouds, and in all weather conditions [3]. The SAR Interferometry (InSAR) remote sensing technique combines two or more radar images to detect changes between acquisitions over the same observed area. It allows for monitoring even slight movement (down to a few millimeters) across wide areas [4]–[6].

Currently, almost all the in-orbit spaceborne SARs are located in Low Earth Orbits (LEO) and are characterized by altitudes typically lower than 1000 km [7]. They have global coverage observation capabilities, but their revisit period over a certain area amounts to several days, leading to high decorrelation [8], [9]. With its daily repetition of the orbit, the Geosynchronous Synthetic Aperture Radar (GEO-SAR) aims to overcome this limitation [10]. Furthermore, the huge distance enables very wide swaths and continental access regions within minutes, capabilities otherwise unavailable even for dense LEO-SARs constellations [11]–[14].

The idea of exploiting a geosynchronous orbit for a synthetic aperture radar was introduced by Tomiyasu in 1978. He proposed a trajectory with a tiny inclination of just 1° that allows for imaging an area of about seven thousand kilometers in North-South and two thousand in East-West [3].

That concept was improved in 1983 by using an orbit with a considerable inclination of about 50° and a small eccentricity that resulted in a big "figure 8" track. Thanks to that inclination, the geosynchronous SAR ground track extends from Buenos Aires to New York, covering about 8500 km, in just a few hours, giving continental coverage with decametric resolution. However, the resulting high velocities demanded large antennas, from 15 to 30 m, and high transmitted power, up to 1 kW on average, are challenging even nowadays, after 40 years [15].

In 1998, Prati et al. proposed a different concept that uses existing broadcasting satellites in low inclination-low eccentricity and geostationary orbits. The very low relative velocity enables long integration times to compensate for huge spread losses, still using moderate powers and antenna size of a few meters [10], [16].

Fig. 1. Footprints of a telecom compatible geosynchronous SAR [11].

Since then, a wide variety of systems has been presented and

Matteo Monti and Andrea Monti Guarnieri are with the Dipartimento di Elettronica, Informazione e Bioingegneria, Politecnico di Milano, 20133 Milan, Italy (e-mail:matteo.monti@polimi.it).

Francesca Pelliccia and Alfredo Renga are with Università degli Studi di Napoli Federico II, 80138 Napoli, Italy.

discussed in the literature, either based on the geosynchronous or the geostationary orbit and their capability to provide images, interferograms, and even tomograms of good quality has been widely demonstrated [10], [11], [17]–[21].

Indeed, the mainstream GEO-SAR concepts mainly include near-zero inclination GEOSARs and inclined GEOSARs. Among the latter schemes, high- and medium-inclination schemes are popular research topics, in which the shapes of the nadir-point trajectories are large and small figure 8 shapes, respectively. The inclined schemes have mainly been studied by scholars from the U.S.A. and China, while most work on near-zero inclination schemes has been carried out by European scholar [7], and are the ones of interest for the present paper since they enable for antenna size and power reduction.

In [22] the impact of Laplace orbit plane property of requiring minimal station-keeping is studied for its potential in long-term geosynchronous synthetic aperture radar (GEOSAR) imaging missions. In The Laplace orbit plane, characterized by an inclination of 7.4° and a right ascension of the ascending node of 0° in the GEO region, the station-keeping fuel requirements are minimized due to the balancing of gravitational perturbations from the Sun and Moon. This makes it a promising candidate for long-term geosynchronous synthetic aperture radar (GEOSAR) missions, as it offers stability and reduced propellant demands. However, strict adherence to the Laplace plane's parameters constrains mission design.

With this paper, we propose a system suitable for the observation of European and Mediterranean areas (i.e., mid-latitude areas) by saving as much as possible in terms of transmitted power and antenna size, but still keeping an adequate azimuth resolution and preserving frequent revisit capabilities.

To do so, a viable configuration is the one provided by the Near-Zero Inclination (NZI) orbital scheme. Challenges associated with NZI GEOSAR, including phase decorrelation, speckle noise, and station-keeping, are analyzed in [23]. This study recommends an inclination around 10^{-3} degrees to have a baseline between subsequent acquisitions under 10% of the critical one along the daily motion, and address cross-track and along-track spectral decorrelation due to orbital drifts caused by perturbations. Optimal station-keeping strategies and periodic maneuvers are derived based on International Telecommunication Union (ITU) orbital box constraints. In [24] the Hydroterra mission, one of the three candidates for ESA's Earth Explorer 10 Program, is introduced. The focus of that work is on two aspects of the system engineering activities performed in the frame of its Mission Analysis and Needs Identification Phase. The authors propose a suitable orbit that provides sub-sidereal interferometric capabilities to the system. Moreover, they describe the methodology used to optimize the acquisition considering the particularities of geosynchronous SAR, thus leading to the derivation of operational scenarios for the system.

The present paper moves from these above-mentioned studies. Its main innovation is two-fold. On one side, a specific set of mission requirements is derived for matching SAR imaging and interferometric applications from a near-zero inclination geosynchronous orbit. Then, a specific orbit control strategy, tailored to operations and able to cope with all the defined requirements is developed.

The intended mission applications are those framed in the cycle of water, discussed in [25], measuring daily and sub-daily variation of water-vapor, soil moisture and deformations, serving meteorology forecasts, hydrologic forecasts of flooding and landslides, irrigation monitoring, and capturing the dynamics of hazardous motion of volcanoes as well as tectonics plates.

For all these applications, sub-continental coverage and coarse-resolution imaging are well within GEO-SAR capability. However, a short revisit interferometric capability is of paramount importance. Indeed, to exploit the potential daily and sub-daily revisit capabilities of this system a tight control of the nominal orbit is mandatory to assure spectral overlap between subsequent acquisitions both in cross-track and along-track directions.

Two approaches have been conceived to perform this task. The Tangential-Normal-Radial (TNR) control approach implies the implementation of maintenance maneuvers in all the directions (i.e., tangential, normal, radial) exploiting four maneuvering points, i.e., perigee, apogee, and nodes, along the ellipse of motion. The Tangential-Normal (TN) control approach, instead, involves only tangential and normal maintenance maneuvers in three maneuvering points, apogee, and nodes. The latter strategy is conceived taking into account the concept of operations of SAR systems in GEO orbit and also aiming at saving propellant mass. Specifically, the Delta-V, ΔV, which represents the velocity change that is required to perform orbital maneuvers [26], is used to characterize propellant usage. A feasibility analysis is conducted to assess the compliance of the two proposed approaches with the assigned mission interferometric requirements.

The paper is organized as follows. In section II, the next one, a comparison between the two different GEO-SAR concepts, the geosynchronous one and the Near Zero Inclination (NZI) geostationary one, is provided. We show that the latter is the most suited for a system with current technologies in terms of available power and antenna size and for covering areas at mid-latitudes, like the ones of the Mediterranean Sea, in which we are interested. We provide guidelines for the orbit design, together with an example of a system with daily revisit over a wide area in the Mediterranean region.

In section III, we show how an NZI mission, whose daily motion is limited to about hundred-fifty kilometers with respect to Earth, is capable of wide area coverage by scanning sub-apertures with a peculiar mode that loosely resembles ScanSAR.

In section IV, we discuss the key performance related to the image quality: the Noise Equivalent Sigma Zero (NESZ) for backscatter-based applications and coherence for the interferometric ones, and how this last imposes stringent requirements on the repetition of the orbit.

In section V, we discuss the orbit control aiming to fulfill the interferometric requirements, and we propose two different methods to control the orbit to comply with the strict interferometric requirements TNR and TN control strategies. The two methods are compared in terms of interferometric

performance and fuel efficiency and conclusions are drawn in the last section VII.

II. GEO-SAR CONCEPTS AND ORBITS

The orbital period of a GEO satellite is equal to the sidereal period of rotation of the Earth, which corresponds to a fixed semi-major axis of about 42164.2 km. The other Keplerian elements impact the shape and location of the orbital ground track projected on the ground.

The argument of perigee ω establishes the angular shift between longitude and latitude histories. For ω equal to 90° and 270°, longitude and latitude, motions are in phase quadrature, and the satellite ground track describes an ellipse aligned with the North-South/East-West Earth axes. The difference between the two cases is that in the former (90°), the Earth-Centered Earth-Fixed (ECEF) satellite motion along the ellipse is clockwise, and in the latter (270°) is counterclockwise. For applications of interest, a correct selection of the argument of perigee is of crucial importance. The reason is linked to the definition of interferometric pairs along the ellipse of motion that needs the longitudinal symmetry of the track with respect to the North-South axis.

The Right Ascension of the Ascending Node (RAAN) is selected to place the orbit at the desired mean longitude. They are related by Greenwich sidereal time that depends on the epoch. The relation between RAAN and mean longitude is expressed in (1)

$$\lambda_0 = \Omega + \omega - \Theta(t_0) + M, \tag{1}$$

where λ_0 is the mean longitude, Ω is the RAAN, ω is the argument of perigee, $\Theta(t_0)$ is the Greenwich sidereal time at epoch t_0 and M is the mean anomaly [27].

The eccentricity rules the longitudinal motion of the track, while the inclination determines the maximum and minimum latitude of the orbit track and, approximately, has no effect on the longitudinal variation.

Different combinations of orbital parameters allow us to obtain several ground-track shapes and, thus, to define in a versatile way the synthetic aperture of the radar and its length, but also the interferometric baseline components.

The GEO-SAR orbits can be divided into two main concepts depending on the inclination value: geosynchronous and geostationary.

A. Geosynchronous

The geosynchronous SAR concepts proposed in the literature are characterized by a high orbital inclination > 15 °, as the one proposed for the first time by Tomiyasu and Pacelli in 1983 [15].

Several other concepts were proposed, differing in orbit parameters like the eccentricity and the argument of perigee, resulting in the different ground track shapes shown in Fig. 2. The most common is "Figure 8", but other shapes were proposed, like the water drop, the ellipse, and the near-circular. The small "figure 8" track in green is the starting concept of the actual track of Ludi Tance-4 01A [28], which is the first geosynchronous SAR satellite ever launched.

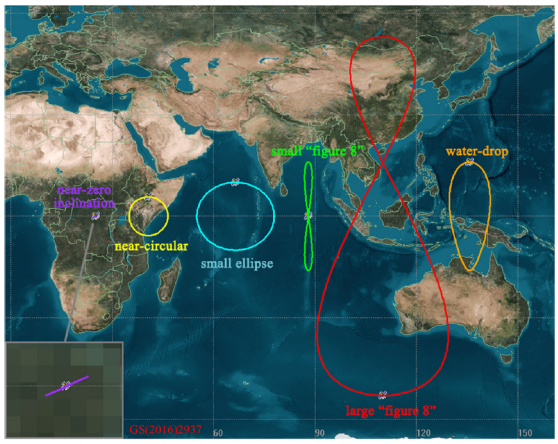

Fig. 2. Geosynchronous SAR configurations, from [7].

The common element of these concepts is the high velocities, with respect to fixed Earth, due to the large inclination, which can be thousands of m/s, as shown in Fig. 3 for a 50° inclined geosynchronous orbit. A large inclination provides huge, near-continental coverage. Conversely, the synthetic aperture time is reduced to a few minutes or less, which limits the ability to achieve sufficient Signal-to-Noise Ratio (SNR) by a small size antenna.

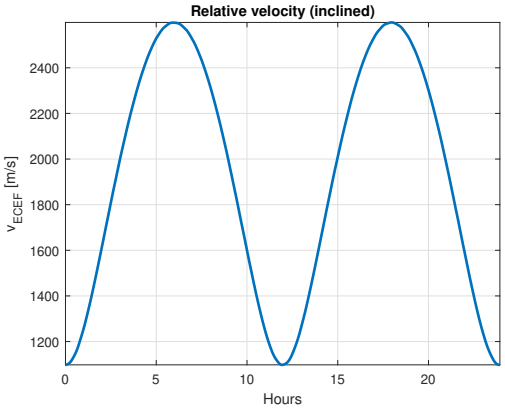

Fig. 3. Norm of the velocity in ECEF frame for a 50° inclined geosynchronous satellite.

B. Geostationary

The geostationary orbit is ruled by the International Telecommunication Union (ITU) Regulation, which manages the satellite allocation slots in terms of both radio-frequency spectrum and GEO belt occupation. In bands shared with terrestrial services, the orbit inclination may need to be determined by inter-service sharing considerations. In other bands, the maximum value is considered up to the natural inclination limit of 15° for satellites launched initially in geostationary or quasi-geostationary orbit if N/S station-keeping maneuvers are not performed [29].

Furthermore, ITU states that space stations on geostationary satellites using frequency bands allocated to the fixed-satellite

service must maintain their position, i.e. the longitude at which the spacecraft crosses the equatorial plane, within a box of $\pm\mathbf{0.1}^\circ$ of longitude of their nominal positions irrespective of the cause of variation. For experimental stations, the box limits can be replaced by $\pm 0.5^\circ$ [30].

The geostationary box is represented in Fig. 4, where, at geostationary distances, $\pm 0.1^\circ$ corresponds to an aperture of approximately 150 km [31] and a latitude extension of $\pm 15^\circ$ is translated to nearly 21000 km.

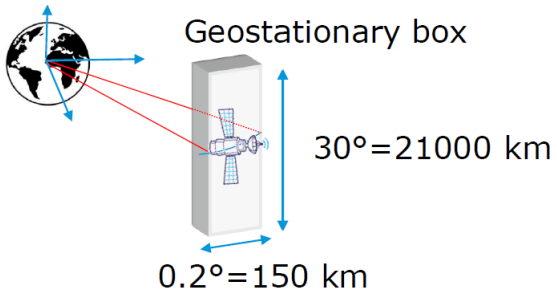

Fig. 4. ITU box for geostationary platforms.

To satisfy the ITU requirements, the eccentricity has to be less than 0.00087 for a slot of $\pm 0.1^\circ$ and 0.0044 for a slot of $\pm 0.5^\circ$. The first GEO-SAR, proposed by Tomiyasu in 1978 [3], has a 1-degree inclined orbit, which makes it compliant with the ITU regulation for geostationary platforms. However, the limitations implied by that tiny inclination, which we discuss here below, were soon removed by evolving the concept into the 50° inclined geostationary SAR published in [15].

In 1998, Prati at. al. proposed a different geostationary SAR, where the orbit has ideally zero inclination, but a small eccentricity was needed to provide a relative Est-West motion that enables the synthetic aperture [16].

The range and azimuth directions of such geostationary, Near Zero Inclined (NZI) orbit SAR were directed respectively along north-south and east-west, so transposed respect to any inclined orbit GEO-SAR concept and also to a conventional LEO-SAR.

The shape of the NZI orbit in an Earth Fixed reference is a small ellipse in the equatorial plane, spanning a longitudinal displacement in degrees of

$$\Delta\lambda = \frac{180}{\pi} 4e. \tag{2}$$

This configuration is characterized by low relative velocities in the order of a few m/s. The low velocity is the crucial parameter that allows for the suppression of thermal noise as well as other noticeable disturbances, like Radio Frequency Interferences and clutter noise [32]–[34]. Figure 5 shows the two different orbital tracks of the Tomiyasu concept with null eccentricity and the NZI concept, together with a synthetic aperture taken after 1 hour of propagation from the perigee.

In Figure 6 the absolute values of the relative velocities of the two geostationary concepts are represented.

The SAR orbit, defined with respect to fixed Earth, determines azimuth and range direction and then the shape of

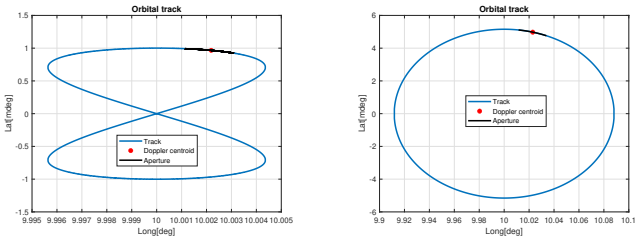

Fig. 5. Orbital tracks of the two main concepts of geostationary orbit. On the left is shown the track of the Tomiyasu concept with eccentricity e = 0. On the right is represented as an example of an elliptical NZI orbit. A synthetic aperture of 1 hour was taken after 1 hour of propagation from the perigee.

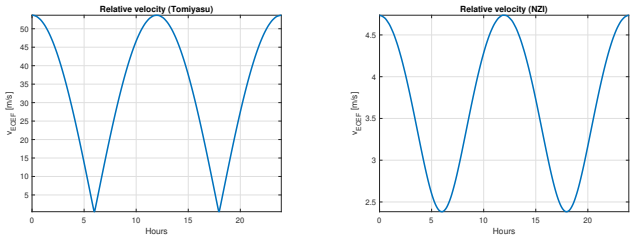

(a) (b)

Fig. 6. Norm of ECEF velocities, along the track, of two geostationary SAR: one (left) with a 1° inclined orbit and eccentricity e = 0, then moving essentially North-South, and one (right) moving essentially East-West, with zero inclination (NZI), but spanning the whole ±0.10 longitude range allowed by ITU.

the resolution cells on the ground. These are represented as iso-range and iso-Doppler lines in Fig. 7 for the 1-degree Tomiyasu with null eccentricity and the NZI geostationary orbits, respectively.

The best performances are achieved when iso-range and iso-Doppler are orthogonal, which limits the observation scenario of the first concept to a very small range of latitudes across the equator. For the NZI configuration, instead, it is possible to observe a wide range of latitudes, similar to a high inclined orbit SAR, but still retaining the benefit of long integration times. The remainder of the paper is thus focused on NZI GEO-SAR only.

C. Geostationary Orbit Design

Orbit elements required to implement the NZI GEO-SAR are herein discussed.

The semi-major axis (a) should be fixed by the orbital period of one sidereal day (i.e., a_s=42164.2 km). However, an increment of semi-major axis, Δa, of 2.1 km is assigned to the nominal orbit to counteract the natural eastward drift that the satellite would immediately experience once disposed of in orbit.

The Argument Of Perigee (ω) determines a sort of squeezing of the shape, maintaining fixed the ratio of the vertical and horizontal dimensions [35]. The chosen value for our application is 90° to get a symmetric longitudinal shape of the track, thus enabling specular acquisitions with respect to the ellipse vertical axis with sub-daily revisit periods.

The Right Ascension of the Ascending Node (Ω) is derived from (1):

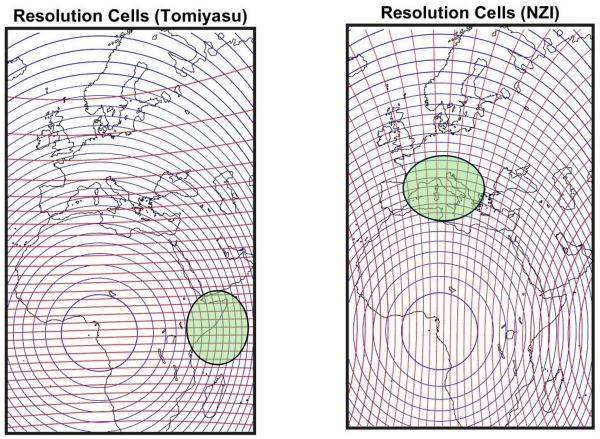

Fig. 7. Iso-range (blue) and Iso-Doppler (red) lines of the two geostationary concepts over Europe and Africa. The mean longitude of the satellite is 10°E. On the left is reported the case for the 1-degree Tomiyasu concept with e = 0. The lines are orthogonal in the equatorial area (see the green zone). On the right is the case of the NZI concept reported. The lines are orthogonal in the North-South direction, allowing observations even at mid-latitudes (see green zone).

$$\Omega = \lambda_0 - \omega + \Theta(t_0) - M. \tag{3}$$

For the case study, the desired spacecraft's mean longitude is 10°E to perform observations around European longitudes. The selected epoch is set on 15 March 2036 00:00:00 UTC and the mean anomaly is assumed as 0° to start orbit propagation from perigee.

The eccentricity (e) and the inclination (i) are the most critical parameters for the optimization of SAR imaging and interferometric performance. The eccentricity is defined as the result of a trade-off analysis between desired imaging performance (i.e., azimuth resolution) and $\pm 0.1°$ box limitation from ITU.

The desired azimuth resolution is defined as 60 m. To guarantee acquisitions with such resolution, the eccentricity has to be accurately tuned to span the desired synthetic aperture in the selected integration time, here considered of 1 hour. As described in [10], the spanned aperture in longitude obtained by considering the perigee as the center can be derived as

$$\Delta\lambda = 4e \sin\left(\omega_T \frac{T_s}{2}\right), \tag{4}$$

where ω_T is the Earth's angular velocity with respect to the fixed stars. Consequently, the aperture is:

$$L_s = 4ea_s \sin\left(\omega_T \frac{T_s}{2}\right), \tag{5}$$

that leads to an azimuth resolution:

$$\rho_{az} = \frac{\lambda}{2L_s} R = \frac{\lambda \cdot R}{8ea_s \sin\left(\omega_T \frac{T_s}{2}\right)}. \tag{6}$$

This rules the relation between resolution and eccentricity. For example, an eccentricity $e = 0.00077$ is needed to achieve an azimuth resolution of 60 m at the perigee (or the apogee).

Finally, the inclination should be ideally zero - as we discussed for the NZI concept [23]. However, it has been shown in [36] that a tiny, non-zero inclination can be used to allow for two interferometric passes in one orbit, attaining a near-zero baseline. This feature is quite relevant since it potentially leads to a sub-daily interferometric revisit that cannot be achieved otherwise unless by using a huge constellation [37], [38].

This sub-daily revisit is achieved by combining symmetric acquisitions with respect to the fixed Earth when the sensor is moving East to West, with those when moving in the reverse direction [39]. A proper tilt of the orbital plane, given by a non-zero value of inclination, induces a sub-daily zero baseline at a desired location on the surface. In Fig. 8 is visually reported the geometry just discussed.

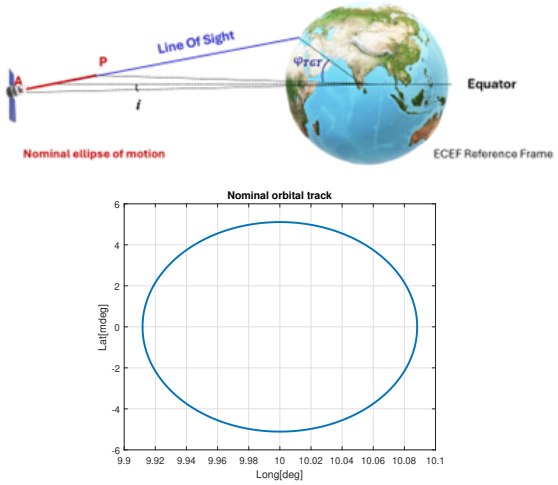

Fig. 8. Example of the geometry for zero-baseline sub-daily interferometry when looking at a specific target on the Earth's surface. On the top is represented the plane tilt needed. On the bottom is reported the nominal orbital ground track of the case of interest.

The required inclination of the orbital plane depends not only on the chosen latitude but also on the eccentricity. Following the same procedure that is discussed in [24], in (7) the relations between the desired latitude, the eccentricity, and the inclination are reported for a target located at a longitude equal to the mean longitude of the orbit:

$$\begin{aligned} R_a^2 - R_p^2 = \\ = 4ea_s^2 - 2a_s r_e[(1+e)\cos(\phi_t + i) - (1-e)\cos(\phi_t - i)] \\ R_a = r_e \cdot \frac{\sin(\phi_t + i)}{\sin(\beta - i)} \\ R_p = r_e \cdot \frac{\sin(\phi_t - i)}{\sin(\beta + i)} \\ \beta = \arcsin\left(\frac{r_e \sin\phi_t}{\bar{R}}\right) \\ \bar{R} = \sqrt{r_e^2 + (a_s(1-e^2))^2 - 2r_e a_s(1-e^2)\cos\phi_t}\ , \end{aligned} \tag{7}$$

where r_e is the Earth's equatorial radius and ϕ_t is the target latitude. By considering the value of eccentricity computed in (6) and a preferred zone of observations located at 43°N, the inclination is designed to be 0.0051°. The target latitude has

been chosen as the mean value between the extreme latitudes of the desired observed area beams.

The nominal orbit parameters are summarized in Table I.

TABLE I
GEO-SAR NOMINAL ORBIT PARAMETERS

Parameter	Value
Semi-major axis (a)	42166.3 km
Argument of Perigee (ω)	90°
Right Ascension of the Ascending Node (Ω)	93.18°
True anomaly (ν)	0°
Eccentricity (e)	0.00077
Inclination (i)	0.0051°
Station Longitude	10°E

The resulting elliptical orbital track in the Latitude-Longitude plane is the one represented in Fig. 5.

III. OBSERVATION SCENARIO

The geostationary SAR here discussed, has a peculiar orbit that is quite different from the approximately rectilinear of LEO-SARs. The GEO-SAR orbit is not all a line, due to the elliptical shape, though the linear approximation holds for a limited aperture [40].

The simplest way to provide observations over a wide area of the Earth for an NZI geostationary SAR is by changing the platform attitude to repoint the antenna in different positions. In this mode, the overall coverage can be extended to all the places of interest. The operating mode is illustrated in an example in Figs. 9 and 10. As Fig. 9 shows, nine sub-apertures have been defined in the first orbital arc, encompassing 12 hours, to cover an area that is extended approximately 3900 km in longitude and 1700 km in latitude. In each sub-aperture, one of the nine footprints shown in 10 is imaged. The footprint is about 400 x 600 km as it results from the pattern of a 6 m antenna and the C band. In the real world, the system will progressively sweep over the different footprints, whereas the proposed representation, made of nine discrete spots, is just provided to simplify the system analysis.

Each footprint is observed by a sub-aperture that lasts for about one hour. In this case, there are two intervals of about 1.5 hours close to the nodes where the system does not acquire since the synthetic aperture would be too small to provide the needed azimuth resolution.

In the second orbital arc, the same set of nine beams is observed to achieve a twice-a-day revisit. The goal is to enable interferometric combinations between the two observations of the same beams within the same sidereal day, and this can be done by ensuring the repetition of the satellite-target angles in the so-called sub-daily interferometric mode discussed in [36].

IV. GEO-SAR PERFORMANCE AND REQUIREMENTS

The huge range heavily penalizes GEO-SAR image quality, which needs to be recovered by long integration times, which in turn exposes the system to further clutter sources [41]. The SNR on the single-look complex image is computed by the Radar equation [11], [42]–[44]:

$$SNR = \frac{P_t G^2 \lambda^2 \eta}{(4\pi)^3 R^4} \frac{\sigma^0 \rho_{az} \rho_{gr} T_s}{N_0}, \tag{8}$$

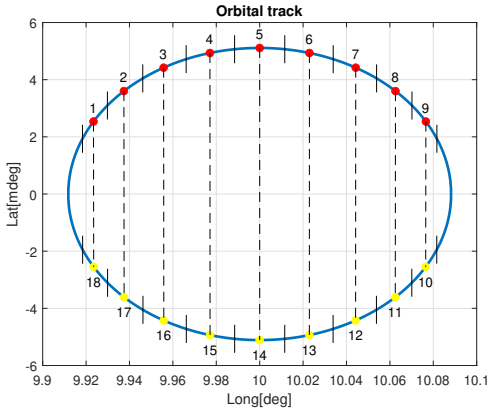

Fig. 9. Representation of the suitable sub-apertures over the orbital track of a NZI ITU compliant GEO-SAR. Each sub-aperture is 1 hour long. Two intervals of 1.5 hours close to the nodes are not considered for the acquisitions due to the apertures being too small to provide the needed azimuth resolution.

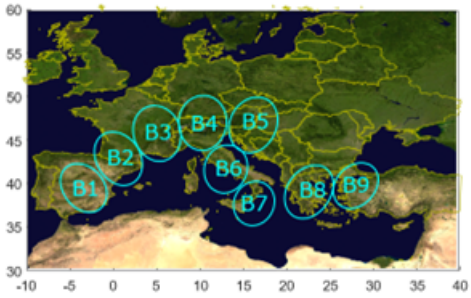

Fig. 10. Example of a possible wide-area coverage achieved by scanning multiple footprints within the same day. Here, each oval corresponds to a single C-band footprint of a circular reflector of 6 m. Each footprint is observed by a different sub-aperture in Fig. 9.

where the terms involved are defined in Table II. The leading term is the dependence on SNR with R^{-4}, which accounts for a loss by a factor of 44^4 with respect to a LEO-SAR orbit, as shown in Fig. 11, that is only partially compensated by the increased integration time.

For a fair comparison between a GEO and a LEO SAR, we assumed in Table II a mean transmitted power, P_t=400 W, and a ground resolution, 15×60 m single look, that closely matches Sentinel-1 Extra Wideswath mode (EW), whereas we set the total noise temperature to a pretty high value, 2500 K, to account for Radio Frequency Interferences and clutter noise that develops in the long integration time [25], [33], [44]–[46].

The integration time, T_s, is ruled by the sensor velocity, hence the orbit eccentricity: a low velocity enables a long integration time, favoring SNR but limiting the system performance in terms of images per day. The ITU-compliant eccentricity discussed in the previous section leads to T_s =1 hour, which provides a gain of about 43 dB with respect to Sentinel-1 EW, which only partially compensates for the increase of spread losses.

However, the NESZ, the most relevant figure of quality for SAR imaging, defined as the backscatter σ^0 that gives unitary SNR, evaluated in (8) results in -21.7 ÷ -15.7 dB at the beam center and at the beam edge, respectively.

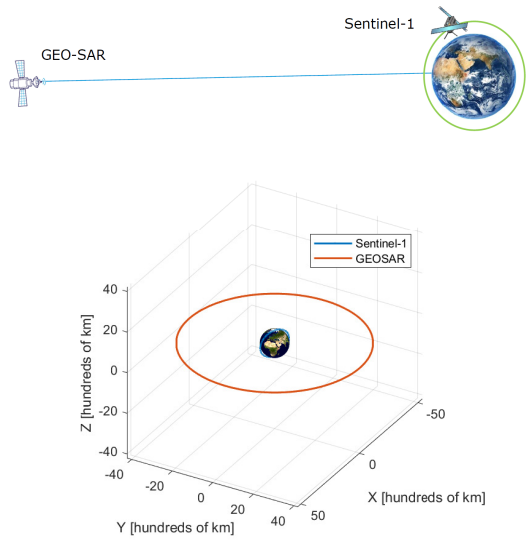

Fig. 11. Comparison between Sentinel-1 and GEO-SAR orbits. On the top is reported a representation of the difference between the orbital distances of LEO-SAR, like Sentinel-1, and GEO-SAR. On the bottom are represented the two different orbits in ECI frame.

TABLE II
GEO-SAR PARAMETERS

Mean transmitted power (P_t)	400 W
Wavelength (λ)	0.056 m
Total losses (η)	-4 dB
Range (R)	37000 km
Incidence angle (θ)	53○
Antenna diameter	6 m
Antenna gain (G): beam center ÷ beam edge	50.6 ÷ 47.6 dB
Maximum speed (v_{sat})	4.7 m/s
Integration time (T_s)	3600 s
Azimuth resolution (ρ_{az})	60 m
Ground range resolution (ρ_{gr})	15 m
Backscatter coefficient σ^0	-14.4 dB
Total noise temperature(T)	2500 K
NESZ: beam center ÷ beam edge	-21.7 ÷ -15.7 dB
SNR beam center ÷ beam edge	7.3 ÷ 1.3 dB

The NESZ has to be compared with the scene backscatter to get the achievable SNR. The values 7.3 ÷ 1.3 dB reported in Tab. II result by assuming the backscatter of Ulaby-Dobson class 'grasses,' at C-band, HH polarization and incidence angle 53^0 [47], and computed at the swath center (best case) and swath edges (worst case). Such values are way worse than those of an LEO-SAR equipped with similar technologies in terms of antenna and power, but they are still acceptable for imaging applications.

As for interferometry, we have to face additional sources of noise that combine. The figure of quality is the absolute value of the coherence between the two repeat-pass images [2], [4]:

$$\gamma = \gamma_{sc} \cdot \gamma_{topo} \cdot \gamma_{th}, \tag{9}$$

where we accounted only for the most relevant decorrelation sources: the scene stability, γ_{sc}, the topographic term, γ_{topo}, and the thermal noise γ_{th}, respectively.

Thermal noise coherence relates to the SNR as follows:

$$\gamma_{th} = \frac{1}{1 + 1/SNR}. \tag{10}$$

As an example, a zero dB SNR results in $\gamma_{th} = 0.5$.

The scene coherence depends on the changes occurring in the interferometric revisit. Its value will depend upon the scene (desert, vegetation, snow, water), the season, the revisit interval, and the wavelength. While water decorrelates in milliseconds, acting as noise in any repeat-pass survey, vegetation stays coherent for days when observed from the C-band. Typical values measured from LEO-SAR missions and corroborated by ground-based observations range from 0.4 to 0.7 for a daily revisit and 0.1 to 0.3 for the 12-days revisit of Sentinel-1 [46], [48], [49]. It is then clear that scene decorrelation impacts LEO-SAR interferometry much more than for GEO-SAR.

The last noise term, the topographic decorrelation, is the one that drives the design of the orbit control since this ultimately imposes that the orbit, expressed in an Earth-fixed reference frame, should be kept within a tight tube, as shown in Fig. 12.

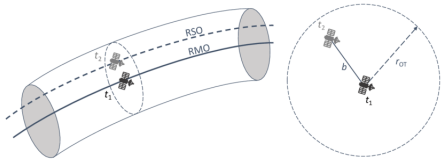

Fig. 12. Sketch of the orbital tube formed around the ECEF reference orbit. The satellite should be controlled to keep that tube.

This requirement comes from the dependence of the topographic coherence and the normal baseline between the two acquisitions, B_n, that is represented in the simplified interferometric geometry of Fig. 13.

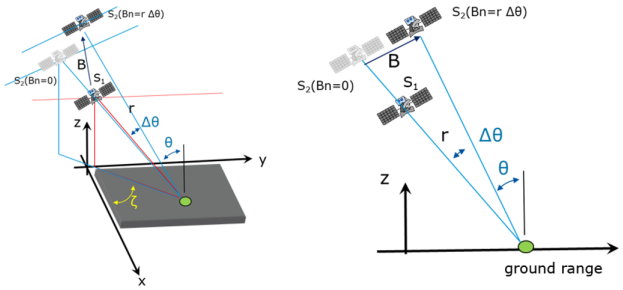

Fig. 13. Geometry of interferometric configuration in the simplified case of straight orbit. Left: in the 3D plane. Right: in the ground range, z-plane.

If the two interferometric acquisitions are taken from positions that differ by a normal baseline, decorrelation arises and it can be evaluated as follows: [2], [4], [50]

$$\gamma_{topo} = \exp\left(-\frac{1}{2}\left(2\pi \cdot \frac{\sigma_q}{h_a}\right)^2\right), \tag{11}$$

where σ_q is the standard deviation of the elevation of the scatterers in the resolution cell, and h_a is the elevation of ambiguity defined as the elevation that causes an interferometric phase shift of 2π

$$h_a = \frac{\lambda R \sin\theta}{2B_n}. \tag{12}$$

As for σ_q, we plotted in Fig. 14 the values of σ_q derived from Copernicus DEM at 30 m resolution, for different types of topography and window sizes. We can state that a value $\sigma_q \simeq 20$ m is a conservative choice for a GEO-SAR with $15 \times 60\ m^2$ resolution.

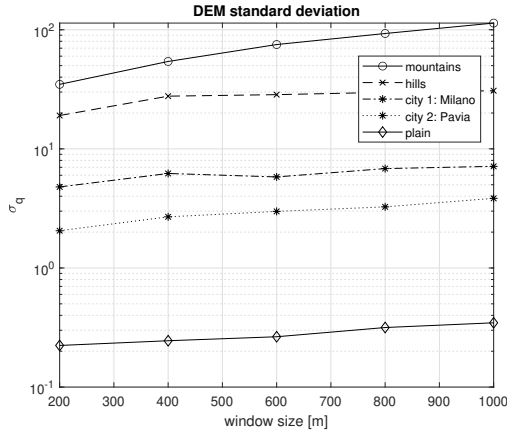

Fig. 14. Standard deviation of the heights estimated from Copernicus DEM GLO 30 over different window sizes and different types of topography.

The overall GEO-SAR coherence, computed for different conditions of SNR and temporal correlation, has been plotted in Fig. 15 as a function of the normal baseline.

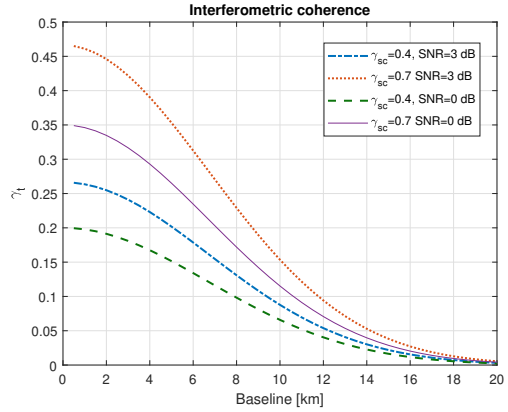

Fig. 15. Interferometric coherence as a function of the normal baseline for different combinations of scene and thermal noise decorrelation.

The achievable interferometric performance lets us draw two major conclusions.

- baselines within 2 km do not impact interferometric performance, whereas baselines above 8 km significantly penalize them. This result is corroborated by the 200 m (3-sigma) orbital tube requirement for Sentinel-1 mission [51] - that scales to $200 \times 44 = 8.8$ km at the GEO orbit.

- as for interferometry, the SNR achieved by the NZI GEO-SAR is well acceptable.

Besides the baseline, a further requirement related to the orbit control should be added for interferometric applications. performance. It should be imposed that the two interferometric acquisitions share a common angular bandwidth in the azimuth direction, $\Delta\psi$, as shown in Fig. 16 [2]. The interferogram resolution is then computed by replacing the synthetic aperture length in 6 with:

$$L_s \simeq R\Delta\psi. \tag{13}$$

As the common band shrinks, the interferogram resolution worsens by the same amount. Then, a good figure for the common band is to match 80-90% of the total azimuth bandwidth.

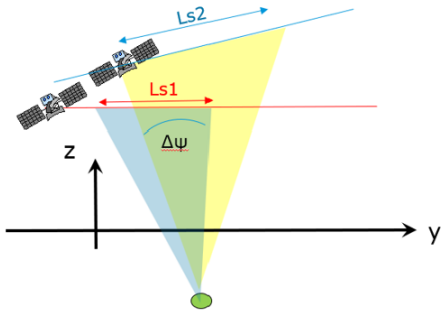

Fig. 16. Exemplification of the common angular bandwidth concept: the two acquisitions overlap for an angle $\Delta\psi$.

V. Orbit Control Strategies

A. Mission Requirements

The C-band near-zero inclination GEO-SAR system shall be compliant with ITU Regulation considering $\pm 0.1°$ in longitude as the reference box dimensions.

The interferometric requirements, instead, are driven by the normal baseline and the common azimuth angular band overlap. In particular, the normal baseline depends on the desired elevation of ambiguity defined in (12). By considering an incidence angle suitable for observations over the Mediterranean area and a reasonable value of 150 m of elevation of ambiguity, the relative requirement on the baseline is given by

$$B_n = \frac{\lambda R \sin\theta}{2h_a} \simeq 5\ km. \tag{14}$$

For what concerns instead of the overlap, the GEO-SAR common band between each acquisition and the reference one, measured during sub-aperture (with an integration time of one hour), should match for 90% of the total azimuth bandwidth to guarantee desired high system performance.

The orbit control strategy should allow all the requirements compliance, so the satellite can keep a narrow orbital tube around the nominal reference trajectory and maintain the track inside the box defined by the ITU regulations by requiring the minimum ΔV during the total mission duration.

As said, a traditional GEO satellite, e.g. a telecommunication satellite, is assigned with a station-keeping (SK) window, a rectangular region above the Earth, whose sides are lines of longitude and latitude. Conventionally, satellites in GEO use chemical propulsion for SK within this window. The propulsion system is manually commanded from the ground to fire roughly once every two weeks to compensate for secular

and periodic perturbations that force the satellite outside of its station-keeping window. SK maneuvers that a GEO satellite performs are typically small, but over an ordinary satellite lifetime of twelve to fifteen years, the total Delta-v required is substantial [52]. SK typically involves East-West (EW) maneuvers, correcting longitude drift and eccentricity, and North-South (NS) maneuvers to maintain inclination. Mainly, the control actions include tangential velocity increments to adjust drift rate and eccentricity (affecting mean longitude), and normal velocity increments to perform inclination changes, according to the derivations in [53]. On average, the total ΔV that is required for traditional missions is in the order of 50 m/s per year [53], [26], and the cost of control is dominated by out-of-plane burns.

The above-discussed, classic approach to the orbit control of a GEO satellite is not suitable for the GEO-SAR case because it keeps the satellite track inside the assigned box, but it does not maintain the shape of the orbit and, consequently, the orbital tube.

For this reason, two different strategies have been conceived. The first one, called TNR (Tangential-Normal-Radial), is based on the idea that the shape of the orbital track can be controlled by performing four maneuvers per day in perigee, apogee, and nodes. Besides the classical tangential and normal maneuvers, radial impulses are applied to adjust the perigee argument and the trajectory's orientation. The second strategy, TN (Tangential-Normal), includes three maneuvers at apogee and nodes. No radial maneuvers are performed in this case.

B. TNR (Tangential-Normal-Radial) strategy design

The idea of the first proposed strategy, the Tangential-Normal-Radial (TNR) one, is to execute maneuvers in four special points along the trajectory, i.e., apogee, perigee, and nodes. A daily-frequency maneuvering cycle has been designed, and maneuvers performed in all the directions – tangential, normal, radial – are exploited as follows.

The first maneuver is a tangential burn applied at the perigee. The purpose is to correct the semi-major axis (i.e., the orbital period) and the eccentricity of the orbit, which determine the longitude extension and drift of the ground track. Given the desired semi-major axis a_t, the specific mechanical energy of the desired new orbit, ϵ_t, is [54]

$$\epsilon_t = -\frac{\mu_\oplus}{2a_t}. \tag{15}$$

where $\mu_\oplus$ is the Earth's standard gravitational parameter. So, the needed impulsive change of velocity can be computed as

$$\Delta V = \sqrt{2\left(\frac{\mu_\oplus}{R_p} - \epsilon_t\right)} - V_p \ , \tag{16}$$

where R_p and V_p are the radius and velocity of perigee of the initial orbit [54].

After the first burn, the satellite is propagated to the descending node, where an out-of-plane burn is performed to correct the inclination. The important point is that this maneuver can be performed at the nodes because the line connecting these points is what the orbit tilt, or inclination, rotates about. The generic equation of ΔV for an inclination change is expressed in the equation below

$$\Delta V = 2V_i \sin\left(\frac{\Delta i}{2}\right), \tag{17}$$

where V_i is the velocity of the orbit before the change of plane [54], [55], and Δi is the required inclination change.

Once at apogee, a combination of two types of burns is applied. The first one is another tangential maneuver like the one at perigee aimed at correcting possible errors in eccentricity and semi-major axis induced by the perturbations or by the previous out-of-plane maneuver. The second one is a radial burn that aims at adjusting the argument of perigee of $\Delta\omega$. The latter can be corrected by using a radial impulse applied at perigee/apogee, where it does not affect other orbital parameters, keeping the correct shape of the orbit [56]. The equation of the impulse needed for this last type of maneuver is presented in the following equation [54]

$$\Delta V = 2\sqrt{\frac{\mu_\oplus}{a(1-e^2)}}\, e \sin\left(\frac{\Delta\omega}{2}\right). \tag{18}$$

The last maneuver is another out-of-plane impulse applied at the ascending node. The purpose is to correct the inclination of the orbit to reach the right position for the perigee. In Fig. 17 are represented the four points in which maneuvers are executed for the designed NZI geostationary track are represented.

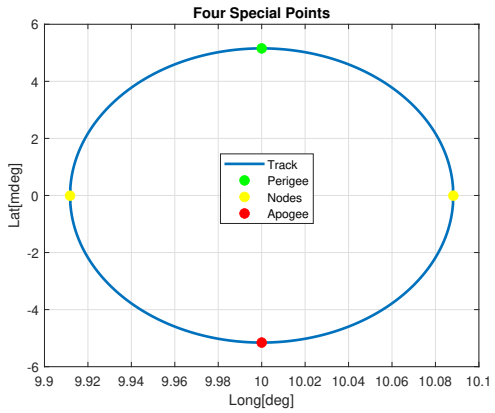

Fig. 17. Orbital track of NZI GEO-SAR with the four special points for the maneuvers.

The main idea of this strategy is to keep the orbit as frozen as possible in correspondence of apogee and perigee by performing maneuvers to reach the desired value of inclination at the apogee (to minimize the sub-sidereal normal baseline) and reaching the desired values of longitude, eccentricity, argument of perigee and inclination at the perigee, where observations can be acquired with the best performance.

C. TN (Tangential-Normal) strategy design

The second control strategy approach exploits the control points in a different way. The rationale is that radial burns are inefficient and they determine most of the maneuvering cost in the TNR strategy. Additionally, these types of maneuvers are

not suitable to restore both the orbit orientation and semi-major axis. Indeed, longitudinal drifts will be allowed in this case, thus compromising the desired azimuth band overlap between subsequent acquisitions. So, the idea of TN strategy is to exploit only tangential and normal maneuvers prioritizing the repetition of the motion conditions in the azimuth plane. The main advantage will be an expected reduction of the required ΔV. This is a crucial aspect in assessing the feasibility of this mission concept. Additionally, since the nodes are not useful for performing GEO-SAR acquisitions, the designed control logic aims at performing the maximum number of the required maneuvers in these points.

The maneuvering cycle is implemented as follows: at the first node, a combined tangential-normal maneuver is performed to counteract both the longitude drift rate, modifying the orbit semi-major axis and the inclination drift. The tangential velocity increment can be computed as in (16) but substituting the radius and the velocity computed at perigee with the ones computed at nodes

$$\Delta V = \sqrt{2\left(\frac{\mu_\oplus}{R_N} - \epsilon_t\right)} - V_N, \tag{19}$$

where R_N and V_N are the radius and velocity at the first node of the initial orbit. The velocity change in the normal direction, instead, can be computed through (17). The affected orbit parameters are inclination, longitude drift rate, and eccentricity. At the orbit apogee, another combined tangential-normal maneuver is applied to restore the line of apses orientation, so the main effect consists of restoring the nominal argument of perigee value. In this case, a small plane change maneuver is performed, since both the inclination and right ascension of the ascending node are affected. The required velocity change can be computed as [57]

$$\Delta V_{pc} = 2 \cdot V \sin\left(\frac{\theta}{2}\right), \tag{20}$$

where θ is the required plane rotation angle that depends on the burn location. For the pure inclination change that is applied at the first node, θ is equal to the required inclination angle variation Δi. Additionally, the tangential contribution of the burn affects orbit eccentricity and semi-major axis, and can be computed as in (19) by substituting R_N and V_N with radius and velocity at apogee. Mean longitude, right ascension of the ascending node, and argument of perigee are related through (1). Forcing the satellite to come back to the same central longitude while keeping the desired orbit track orientation implies that the line of nodes has to vary accordingly to satisfy the relation, i.e., the right ascension of the ascending node varies depending on the constraints applied to the argument of perigee and mean longitude.

At the second node, another pure tangential maneuver is required to complete the longitude drift rate compensation and the eccentricity correction. Again, the required ΔV can be computed through (19).

It is worth noting that in this strategy, each maneuver is not applied to restore the nominal orbit parameter of interest at the burn location; it is applied to restore the desired parameter value at the orbit perigee instead. In this case, the idea is to keep the orbit as frozen as possible at this point, that is the preferred acquisition location since here the spacecraft reaches its maximum velocity, which translates into improved imaging performance.

VI. Orbit control implementation and Results

A. Orbit Control Simulation

The selected software for the control strategies simulation is the General Mission Analysis Tool (GMAT), developed by NASA [58]. The orbit definition and propagation are operated in the True Of Date (TOD) reference frame to properly consider the actual contributions of the Earth motion precession and nutation, and the correct perturbing accelerations values referred to the selected epoch that is 15 March 2036 00:00:00 UTC. The terms of the Earth's gravitational potential series development are considered up to degree 21 and order 21. The other celestial bodies whose gravitational attraction affects the satellite motion are the Moon and Sun. As for the solar radiation pressure model, the reflectivity coefficient is considered as $C_r = 1.8$, and the Area-to-mass ratio is defined as $A/m = 0.025\,\mathrm{m}^2/\mathrm{kg}$. The simulation period is equal to one year.

The provided formulation of the maintenance maneuvers' design and planning problem for a GEO-SAR system is based on an orbit propagation model operated through GMAT software and does not take into account errors in satellite state estimation. So the orbit found by integrating the equations of motion in GMAT is considered as both actual and measured orbit. Indeed, in a real-world implementation, measures of spacecraft state vector or equivalently of the orbit elements are derived by an orbit determination tool that can run either onboard or on the ground. The results presented in this section are thus representative of a real-world case as long as precise knowledge, e.g. on the scale of meters, of satellite orbit is available to compute the required ΔV for each maneuver [59]. This implies a precise knowledge of the true orbit observed continuously in real-time during the simulations.

B. InSAR feasibility analysis

1) TNR: in this section, the results of the controlled orbit propagation will be provided considering the first control strategy.

In Fig. 18 the controlled orbit in a topocentric frame centered in the center of Beam B5 of Fig. 10 is represented. Specifically, the reference frame is the local geodetic East-North-Up (ENU) coordinate system. It defines a three-dimensional, right-handed Cartesian coordinate system centered at a specific point on the Earth's surface. The axes are oriented as follows: the East (E) is tangential to the Earth's surface, pointing towards the east; the North (N) is tangential to the Earth's surface, pointing towards the north; the Up (U) is perpendicular to the Earth's surface, pointing outward from the center of the Earth [60].

As it can be seen in Fig. 19, the TNR-controlled ground track differs from the nominal one because of longitudinal shifts of the orbit, that reach the maximum amplitude around

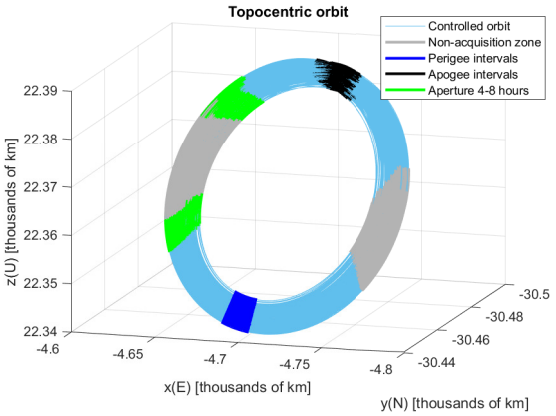

Fig. 18. TNR controlled orbit evolution in the topocentric frame centered in the target B5 over 365 days. Together with the zones of non-acquisition, the couples of acquisition, perigee-apogee, and 4-8 hours from perigee, are represented

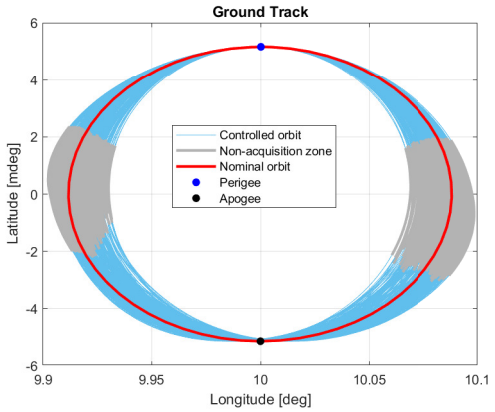

Fig. 19. TNR orbital track evolution in latitude and longitude over 365 days. The principal effect is a slight longitudinal drift with respect to the nominal trajectory.

the nodes. At perigee and apogee, an accurate motion repetition is guaranteed.

The required ΔV budget has been computed for the total simulation duration of one year, and it is reported in Table III by splitting the contribution of each maneuver.

TABLE III
YEARLY ΔV BUDGET ACHIEVED BY THE TNR METHOD

	m/s
ΔV_1	2.9
ΔV_2	23.1
ΔV_3	113.3
ΔV_4	23.4
ΔV_{tot}	162.66

As expected, the first maneuver, which is purely tangential, is the least expensive, while the ΔV of the second and the fourth maneuver is one order of magnitude higher than the first one since the out-of-plane burns are inefficient and determine a higher cost. The radial burn is the most demanding one with a value of ΔV one order of magnitude higher than the North-South correction maneuvers.

Representations through histograms are chosen to compare the interferometric performance over different targets. The selected targets on the ground are the centroids of Beam B1, B5, and B9, represented in Fig. 10. The selected acquisition pairs are 5-14 and 9-10 (Fig. 8). In Fig. 20 the histograms of daily and sub-daily normal baselines are reported.

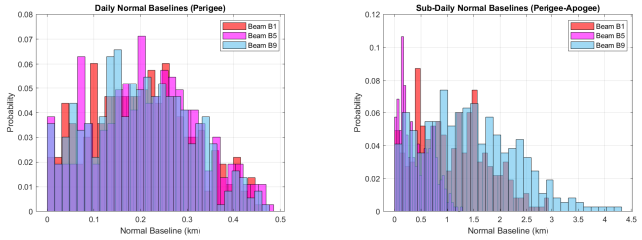

Fig. 20. Histogram of daily (left) and sub-daily (right) normal baselines computed over 365 orbits controlled through TNR strategy. The baselines have been computed by assuming that the satellite acquires images at the perigee for the daily acquisitions, and apogee for the sub-daily ones, and the targets are at the centers of beams B1, B5, and B9 of Figure 10.

In the daily case, the results are quite interesting because, for all the targets, the baseline is always kept under 0.5 km. These values increase in the sub-daily case. When looking at Beam B5, the baselines reach values even around 1 km, while in the cases of Beam B1 and B9, the values rise up to 3 km and 4.5 km, respectively. These are anyway good results because the strategy can keep the baselines under the constraint of 5 km for all the simulations.

In Fig. 21 the histograms of the angular bandwidth overlap percentage over the three different targets are reported.

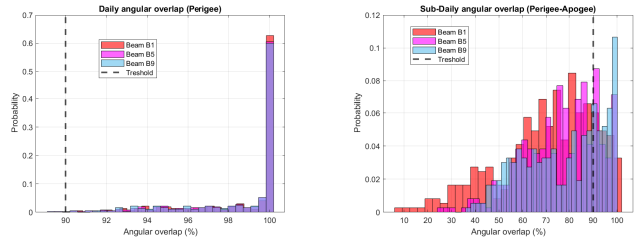

Fig. 21. Histogram of daily (left) and sub-daily (right) angular overlap computed over 365 orbits controlled through TNR strategy. The overlaps have been computed by assuming the satellite at perigee for the daily acquisitions, and apogee for the sub-daily ones, and the target at the centers of the beams B1, B5, and B9 of Figure 10.

TABLE IV
TNR OVERLAP RESULTS (PERIGEE-APOGEE)

	Acquisitions with Overlap $\geq$ 90%
Daily B1	99.45%
Daily B5	99.45%
Daily B9	99.45%
Sub-daily B1	17.76%
Sub-daily B5	23.22%
Sub-daily B9	31.97%

The results show that the orbit is kept really stable at perigee, with nearly 99% of the acquisitions with overlap higher than 90%. However, this strategy does not assure the desired orbit stability at the apogee, meaning that the angular

bands are more shifted with respect to each other and with respect to the nominal one at perigee. This translates in values of overlap even lower than 30%. This issue can be noticed also in Table IV, where the 90% of needed overlap is guaranteed in the beams only for approximately 18%, 23%, and 32% respectively.

The same analysis has been performed for the other couple of points of acquisitions, i.e. the centroids located after 4 and 8 hours from the perigee (the primary point is Point 9 of Fig. 8). In Fig. 22 and 23 the results in terms of normal baselines and azimuth band overlap distribution are reported.

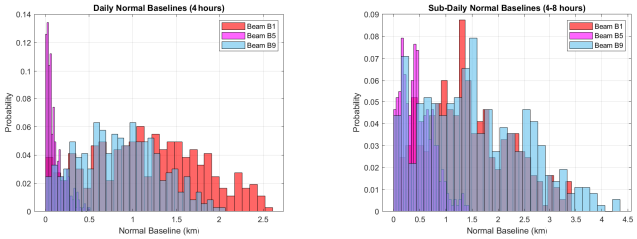

Fig. 22. Histogram of daily (left) and sub-daily (right) normal baselines computed over 365 orbits controlled through TNR strategy. The baselines have been computed by assuming the satellite at 4 hours from perigee for the daily acquisitions, and at eight hours from perigee for the sub-daily ones, and the target at the centers of the beams B1, B5 and B9 of Fig. 10.

In this case, worse performance is achieved. The daily baselines in the previous case were always under 0.5 km, but for this second pair, they achieved values up to 2 km and 2.5 km for Beam B9 and Beam B1, respectively. In the sub-daily case, instead, the values are, on average, higher, but the maximum values are approximately in the same order, around 1.5 km for Beam 5 and 3.5 and 4.5 km for Beam B1 and B9.

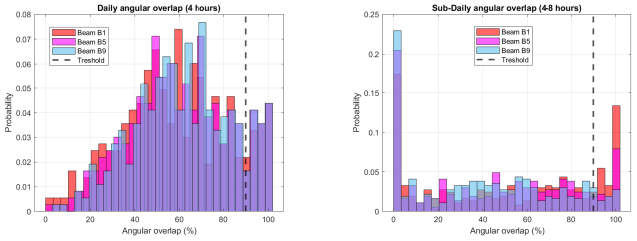

Fig. 23. Histogram of daily (left) and sub-daily (right) angular overlaps computed over 365 orbits controlled through TNR strategy. The overlaps have been computed by assuming the satellite at 4 hours from perigee for the daily acquisitions, and at eight hours from perigee for the sub-daily ones, and the target at the centers of the beams B1, B5 and B9 of Fig. 10.

TABLE V
TNR OVERLAP RESULTS (4-8 HOURS)

	Acquisitions with Overlap $\geq$ 90%
Daily B1	12.88%
Daily B5	13.15%
Daily B9	13.42%
Sub-daily B1	23.50%
Sub-daily B5	13.39%
Sub-daily B9	8.20%

By looking at the overlap results, the impact of the mentioned longitudinal drifts is evident. Values of overlap under 10% are achieved even in the daily case, and in the sub-daily case, the majority of the acquisitions have a null overlap percentage between the two azimuth angular bands. This can be seen also in Table V. In the daily case, for all the different targets, only 13% of the acquisitions are performed in good interferometric conditions. The result is different in the sub-daily case; Beam 1 has the higher percentage of good acquisitions which is 23.5%, while Beam 9 has the worst performance with only 8.2%.

2) TN: As in the previous subsection, the controlled orbit, together with non-acquisition zones and relevant sub-apertures for the TN control strategy case,e are represented in Fig. 24.

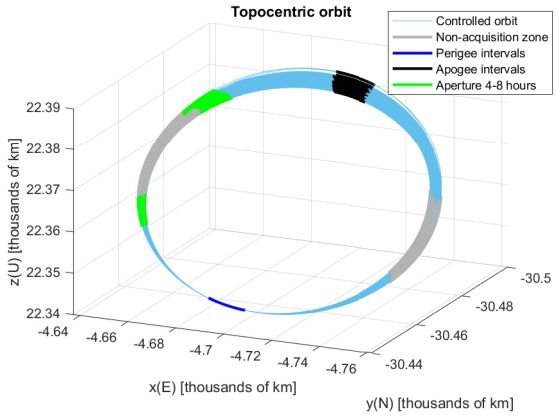

Fig. 24. TN controlled orbit evolution in the topocentric frame centered in the target B5 over 365 days. Together with the zones of non-acquisition, the acquisition pairs, perigee-apogee, and centroids at 4-8 hours from perigee, are represented.

In Fig. 25, instead, the controlled ground track is represented and compared with the nominal unperturbed orbit. The orbit portion around the perigee is maintained nearly frozen with respect to the ideal case. As can be seen, the orbit is free to modify mainly in the portion around the apogee. This is because the nominal inclination is not restored at this point, thus latitude drifts are allowed. The controlled ground track deviates much more from the nominal one, if compared to the case represented in Fig. 19, so it seems that this logic does not lead to a concrete improvement with respect to the first strategy in terms of accurate motion repeatability. However, normal baseline and Doppler bandwidth overlap are the real indicators for the evaluation of the system's interferometric performance. And, as shown later, the results are promising from this point of view.

The budget of ΔV required for one year to control the orbit through TN strategy is reported in Table VI.

TABLE VI
YEARLY ΔV BUDGET ACHIEVED BY THE TN METHOD

	m/s
ΔV_1	30.8
ΔV_2	42.1
ΔV_3	17.3
ΔV_{tot}	90.2

As it can be seen in Table VI, all the maneuvers are of the same order of magnitude in terms of required cost. As

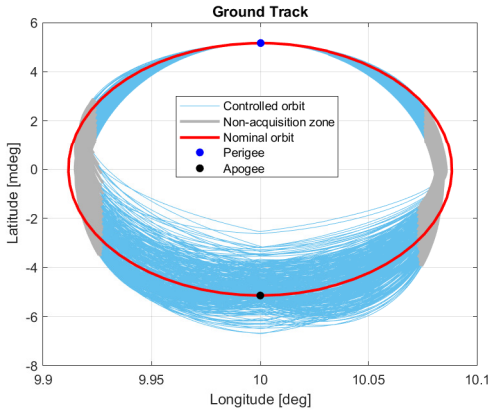

Fig. 25. TN orbital track evolution in latitude and longitude over 365 days. The main effect is a latitude drift with respect to the nominal trajectory in the orbit portion around the apogee.

expected, the most expensive control actions involve plane change maneuvers. The total budget is lower if compared to the TNR strategy since radial burns are avoided in this case.

Among the two control strategies, the TN one requires the minimum maintenance cost, 55% less than the TNR one.

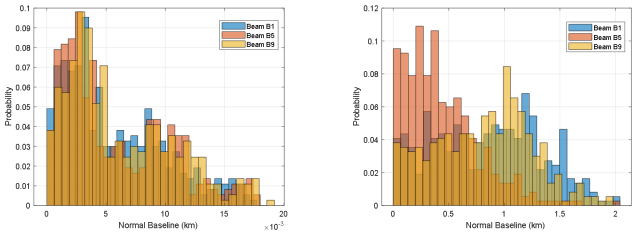

Fig. 26. Histogram of daily (left) and sub-daily (right) normal baselines computed over 365 orbits controlled through TN strategy. The baselines have been computed by assuming the satellite at perigee for the daily acquisitions, and apogee for the sub-daily ones, and the target at the centers of the beams B1, B5, and B9 of Fig. 10.

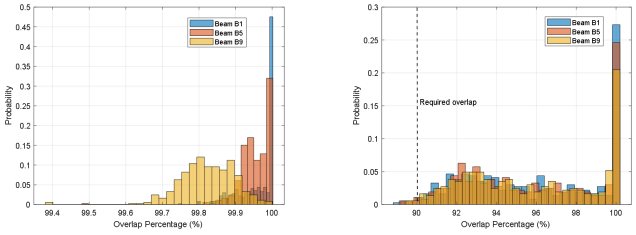

Fig. 27. Histogram of daily (left) and sub-daily (right) angular overlap computed over 365 orbits controlled through TN strategy. The overlaps have been computed by assuming the satellite at perigee for the daily acquisitions, and apogee for the sub-daily ones, and the target at the centers of the beams B1, B5, and B9 of Fig. 10.

The interferometric performance over the same targets of interest has been evaluated considering the TN-controlled trajectory. As it can be seen in Fig. 26, 29, the acquisitions performed at perigee are the best ones in each case since the relative geometry is accurately repeated day by day at this point of the ellipse of motion. In all the selected beams, it

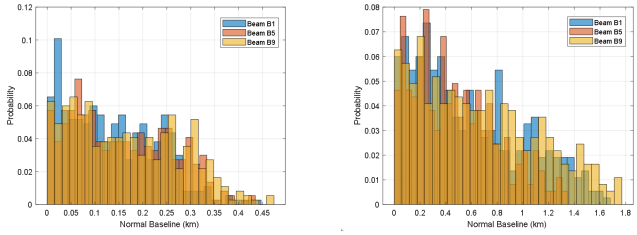

Fig. 28. Histogram of daily (left) and sub-daily (right) normal baselines computed over 365 orbits controlled through TN strategy. The baselines have been computed by assuming the satellite at 4 hours from perigee for the daily acquisitions, and at eight hours from perigee for the sub-daily ones, and the target at the centers of the beams B1, B5 and B9 of Fig. 10.

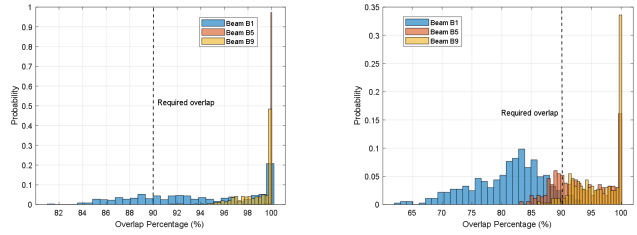

Fig. 29. Histogram of daily (left) and sub-daily (right) angular overlaps computed over 365 orbits controlled through TN strategy. The overlaps have been computed by assuming the satellite at 4 hours from perigee for the daily acquisitions, and at eight hours from perigee for the sub-daily ones, and the target at the centers of the beams B1, B5 and B9 of Fig. 10.

is possible to make coherent acquisitions during the entire simulation period with a 24-hour revisit performing image acquisitions at the perigee, as it is evident in Table VII.

From the point of view of the normal baseline, the interferometric requirement is always met, and the baseline value for the daily revisit acquisitions at perigee is the lowest one, in the order of a few meters. Indeed, the TN frozen ellipse control strategy is designed to optimize the performance at this point, this is possible by requiring that all the nominal orbit parameters are restored here with high accuracy. The acquisitions at apogee, even if characterized by a significantly higher normal baseline value, are still useful for the formation of interferograms. The normal baseline is always well below the imposed threshold value of 5 km. Overall, considering the total number of useful acquisitions computed for the perigee-apogee pair, it is possible to state that each beam can be coherently observed for almost the entire duration of the simulated mission.

Considering the acquisition pair 4-8, it is possible to observe a drastic worsening of the interferometric performance over B1. The useful acquisitions at the second acquisition point of the pair, i.e., the one that is 8 hours away from the current perigee, are equal to 13, which corresponds to 3.55% with respect to the total acquisition opportunities, as reported in Table VIII. Therefore, for almost the entire simulation duration, the azimuth angular band of the slaves does not overlap sufficiently with that of the master. In general, the acquisitions performed at the centroids of the sub-apertures furthest from the perigee in the right side of the motion ellipse, are not suitable for the observation of the westernmost beam

of the observation scenario. Instead, the performance over B5 and B9 is very good, even if worse if compared to the 0-12 pair. The best ones are obtained for beam B9, which is the easternmost beam of the observation scenario. For all the analyzed cases, the normal baseline of the sub-daily scenarios is always in the order of 1-2 km.

TABLE VII
TN OVERLAP RESULTS (0-12 HOURS)

	Acquisitions with Overlap $\geq$ 90%
Daily B1	100 %
Daily B5	100 %
Daily B9	100 %
Sub-daily B1	98.63 %
Sub-daily B5	98.63 %
Sub-daily B9	99.18 %

TABLE VIII
TN OVERLAP RESULTS (4-8 HOURS)

	Acquisitions with Overlap $\geq$ 90%
Daily B1	72.1 %
Daily B5	100 %
Daily B9	100 %
Sub-daily B1	3.55 %
Sub-daily B5	70.22 %
Sub-daily B9	94.81 %

C. Interferometric Revisit Summary

To assess compliance with the interferometric requirements, the acquisition strategy has been selected. In this case study, two different pairs of acquisition points have been considered. One pair exploits perigee and apogee to perform acquisitions. The master image is identified as the image acquired at the perigee of the first simulated orbit. The slave images, instead, represent all the acquisitions performed at the orbit perigee and apogee during the total simulation time of one year. The second pair exploits the last useful points on the right side of the ellipse of motion to perform image acquisitions: the first point is 4 hours away from the orbit perigee, and the second point is 8 hours away from the orbit perigee. The pair is indicated as 9-10. The master image is identified as the image acquired at the first acquisition point of the first simulated orbit. Beam 1, Beam 5, and Beam 9 of the observation scenario are selected to perform the interferometric analyses. Over the zones of interest, a total of 732 acquisitions can be potentially performed in one year.

TABLE IX
TN CONTROL STRATEGY RESULTS: MEAN AND STANDARD DEVIATION OF THE NORMAL BASELINE.

	μ_5	σ_5	μ_{14}	σ_{14}
B1	0.006 km	0.004 km	0.9 km	0.5 km
B5	0.006 km	0.004 km	0.9 km	0.5 km
B9	0.006 km	0.004 km	0.9 km	0.5 km

The two control strategies can be compared in both daily and sub-daily revisit scenarios considering the two requirements separately. In Tables IX, X, XI, XII, mean, and standard deviation of the normal baseline distribution are reported for TN strategy and TNR strategy, respectively. In the mentioned tables, mean μ_i and standard deviation σ_i are related to the acquisition performed at centroid i, where i can be 5,14,9, or 10. For both cases, the normal baseline is always well below the imposed threshold of 5 km, and the TN strategy exhibits better performance for the daily revisit scenario. Indeed, the mean normal baseline that is established at the orbit perigee day by day is in the order of 6 meters. This is due to the accurate repetition of the ellipse of motion in the orbit portion around the perigee. However, the main difference between the two strategies can be appreciated in Tables XIII, XIV. In the mentioned tables, N_i is the number of useful acquisitions related to the centroid i, where i can be 5, 14, 9, or 10. The total number of useful acquisitions, N_{i+j}, where i can be 5 or 9, and j can be 14 or 10, is computed by considering the sum of N_i and N_j to evaluate the performance with respect to the total acquisition opportunities for the selected pair. The results demonstrate that TNR control logic does not enable the sub-daily revisit capabilities of the system, especially when the satellite moves away from the orbit apogee. There are few

TABLE X
TN CONTROL STRATEGY RESULTS: MEAN AND STANDARD DEVIATION OF THE NORMAL BASELINE.

	μ_9	σ_9	μ_{10}	σ_{10}
B1	0.4 km	0.5 km	0.6 km	0.4 km
B5	0.4 km	0.5 km	0.5 km	0.3 km
B9	0.4 km	0.5 km	0.7 km	0.5 km

TABLE XI
TNR CONTROL STRATEGY RESULTS: MEAN AND STANDARD DEVIATION OF THE NORMAL BASELINE.

	μ_5	σ_5	μ_{14}	σ_{14}
B1	0.20 km	0.11 km	1.1 km	0.66 km
B5	0.21 km	0.11 km	0.42 km	0.29 km
B9	0.20 km	0.11 km	1.42 km	0.88 km

TABLE XII
TNR CONTROL STRATEGY RESULTS: MEAN AND STANDARD DEVIATION OF THE NORMAL BASELINE.

	μ_9	σ_9	μ_{10}	σ_{10}
B1	1.17 km	0.64 km	1.39 km	0.8 km
B5	0.11 km	0.10 km	0.45 km	0.3 km
B9	0.85 km	0.46 km	1.55 km	0.98 km

TABLE XIII
TN CONTROL STRATEGY RESULTS: NUMBER OF USEFUL ACQUISITIONS.

	N_5	N_{14}	N_{5+14}	N_9	N_{10}	N_{9+10}
B1	366/366	366/366	732/732	264/366	13/366	277/732
B5	366/366	366/366	727/732	366/366	257/366	623/732
B9	366/366	366/366	729/732	366/366	347/366	713/732

TABLE XIV
TNR CONTROL STRATEGY RESULTS: NUMBER OF USEFUL ACQUISITIONS.

	N_5	N_{14}	N_{5+14}	N_9	N_{10}	N_{9+10}
B1	364/366	65/366	429/732	47/366	86/366	133/732
B5	364/366	85/366	449/732	48/366	49/366	97/732
B9	364/366	117/366	481/732	49/366	30/366	79/732

sub-daily revisit acquisition opportunities for both acquisition pairs. This is due to the shifts of the orbit in the azimuth plane that compromise the angular band overlap between subsequent acquisitions. The TN strategy, instead, enables several acquisition opportunities along the total simulation time of one year. In particular, almost all the performed acquisitions at perigee and apogee are useful to form coherent interferograms over all the selected beams.

Worse performances are achieved by exploiting the 9-10 acquisition pair, especially over beam B1. Overall, it is possible to conclude that the TN control strategy is suitable for the implementation of the NZI GEOSAR system in the context of sub-daily revisit InSAR applications. The direct implication of the obtained results is that it could be possible to restore the nominal orbit parameters with a lower accuracy with respect to the assigned one, obtain errors of a few km in the determination of the baseline vector, and still be compliant with the assigned requirements.

D. Fuel Efficiency Considerations

As an outcome of the performed simulations, an estimate of the required DeltaV is obtained. Considerations are herein reported about the relationships between the computed DeltaV values and the involved propellant mass and fuel consumption. The analysis is based on some assumptions recalled in the following. As for the fuel efficiency considerations, some assumptions that have been considered for the simulations' setting have to be recalled.

1) For a GEO satellite that is characterized by an orbital period of one sidereal day, maneuvers that last a few seconds or even a few minutes can be considered impulsive [59]. The assumption of impulsive burn is compatible with the type of propulsion technology that we imagine when designing the GEOSAR control strategy, which is the chemical one. So, all the control actions are intended to be executed with chemical thrusters that nominally provide high thrusts in short times. Consequently, all the maneuvers are modeled as impulsive burns in a GMAT environment. This is valid for both TNR and TN control strategies. This assumption is important when comes to the application of the Tsiolkovsky equation [61], presented later on. Furthermore, it implies that the required control actions are much shorter (in the order of seconds) if compared to the duration of individual SAR acquisitions, which last for about one hour. Therefore, one can assume that the system will be never asked to collect SAR data while a maneuver is realized.
2) Spacecraft mass, exposed area to the Sun, and reflectivity coefficient are the same for both control strategies. This implies that the effects of solar radiation pressure are the same in both cases, as well as the gravitational attraction between the spacecraft and other orbiting bodies. This choice is made to conduct analyses and comparisons between the two control strategies under the same perturbing conditions. The spacecraft mass value is crucial when evaluating fuel efficiency; for the simulations, it is equal to 2000 kg [25]. This value is thus considered the total wet mass of the spacecraft.

The comparison between the two control logics from the fuel efficiency point of view can now be carried out. The total computed ΔV that is needed during the total simulation time of one year can be translated into total propellant consumption through the Tsiolkovsky equation [61]

$$\Delta V = I_{sp} g_0 \ln\left(\frac{m_0}{m_f}\right),$$

where I_{sp} is the specific impulse in seconds, g_0 is the standard gravity, m_0 is the wet mass, and m_f is the final dry mass. So, the propellant mass, m_p, which is the mass difference between the wet mass and the dry mass, needed to impart the impulsive velocity change, can be derived as follows

$$m_p = m_0 - m_f = m_0\left(1 - \exp\left(-\frac{\Delta V}{I_{sp} g_0}\right)\right).$$

The specific impulse is an indicator of fuel efficiency. Higher values of specific impulse imply more thrust for the same amount of propellant. Depending on the selected propulsive technology and propellants, this value can vary by one order of magnitude. For chemical propellants, it can be considered that I_{sp} varies between 250 and 460 seconds [62].

Once determined the required ΔV to perform maintenance maneuvers, the propellant mass trend as a function of the specific impulse can be derived. In Fig. 30 this trend is represented for the two control strategies. As expected, higher ΔV values imply higher fuel consumption considering the same spacecraft wet mass value. In Fig. 31 the trend of the consumed propellant mass is derived considering 300 s of specific impulse. For each day, the total required ΔV is derived as the sum of the ΔV contribution of each maneuver, this is done for both control strategies. Every day the total consumed fuel by the TNR strategy is almost double the one that is required by the TN strategy. The main contribution to this consumption difference is because the required velocity change of the former is one order of magnitude higher with respect to the latter, thus resulting in a greater required propellant mass. Indeed, the mean value of this distribution is 0.30 kg for the TNR control strategy, and 0.17 kg for the TN one. The total consumed fuel that is needed for a one-year mission is equal to 110.5 kg in the first case, and 61.3 kg for the second case.

VII. Conclusion

The GEO-SAR is an innovative concept characterized by unique observing capabilities that can guarantee daily and sub-daily imaging and continuous measurement of fast motion measurement. The high-altitude orbit allows for huge ground swaths, but penalizes SNR. This issue can be solved using very long integration times, which in turn means low along-track velocity. It is shown that the NZI geostationary concept is the most suited to achieve decametric resolutions that are suited for applications like water vapor, hydrological landslides, irrigation, and deformations monitoring over a wide scale. SAR Interferometry is the enabling technique for such applications, and the NZI configuration allows for a sub-daily revisit suited for the observation of the mentioned fast-evolving phenomena.

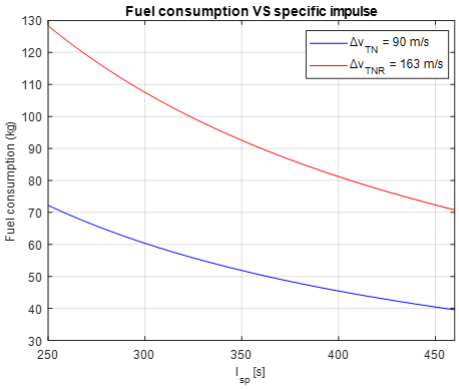

Fig. 30. Propellant mass as a function of specific impulse, comparison between TNR and TN control strategies.

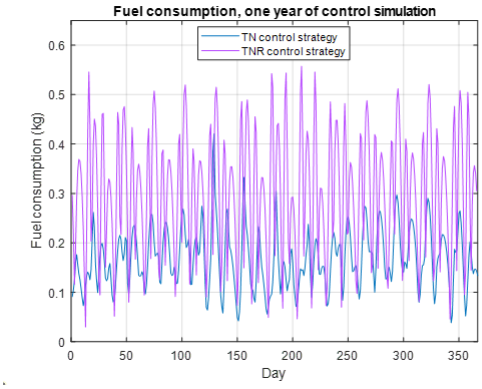

Fig. 31. Trend of the fuel consumption of GEOSAR satellite, comparison between TNR control strategy and TN control strategy, a specific impulse of 300 s is assumed.

In the paper, the design of an interferometric NZI geostationary SAR has been carefully addressed. It has been shown that the requirement for the normal baseline and the common bandwidth imposes severe constraints on the design and control of the orbit. Two control strategies have been proposed and compared, to maintain the shape of the orbital track to keep the orbit tube and the azimuth angular band overlap.

The first one, TNR, is derived from the classical telecommunication satellite control but adds a radial maneuver to keep the orbit shape and orientation. It consists of four daily maneuvers: one purely tangential, two purely normal, and one combined tangential-radial maneuver. This strategy results very well in keeping the daily baseline close to the perigee. However, it causes a drift in longitude that affects the band overlap, far from the perigee. Furthermore, the cost for the radial maneuver is the most impacting one, resulting in an overall ΔV budget of 162 m/s per year.

The TN strategy, instead, is characterized by three different maneuvers: two are combined tangential-normal maneuvers, and the last one is purely tangential. In this case, the idea is to exploit only small plane changes and tangential drift rate compensations according to the inter-dependencies existing between all the orbital parameters. This logic prioritizes the relative motion condition repeatability in the azimuth plane, leaving latitude drifts in the cross-track direction. This results in very good interferometric performance, especially for the very critical azimuth band overlap constraint. The crucial aspect is that this strategy allows the reduction of the total mission cost by avoiding the implementation of radial burns. The total budget is equal to about 90 m/s, which is higher compared to traditional ones but in the same order of magnitude. Additionally, the same type of maneuvers, i.e., tangential and normal maneuvers, are exploited to control the orbital parameters. So, onboard thrust configurations similar to those of traditional GEO satellites can be implemented, leading to similarities in the required platform resources.

In conclusion, it is worth noting that the proposed control strategies tailored for the GEO-SAR system exploit very frequent maneuvers every day, deviating from the standard procedures of GEO satellites. In particular, the typical station-keeping schedule of such satellites includes several segments, such as the orbit tracking segment and the orbit determination and analysis segment, which nominally require times of at least 1 or 2 days [53]. Consequently, the proposal of a control strategy that includes daily maneuvers every 6 or 12 hours is incompatible with the standard procedures that are based on on-ground control of the satellite platform. The most critical issue concerns the accuracy with which orbit determination must be performed. Indeed, compared to traditional GEO missions and station-keeping schedules, GEO-SAR missions require unprecedented orbit determination precision, at least in the scale of meters [63], so novel techniques that can provide these performances are of interest in this context and should be explored to complete the discussion.

Furthermore, alternative propulsion solutions could be also investigated, such as the electric propulsion one. Indeed, the use of electric propulsion systems is being considered as a viable alternative to classical chemical actuators and is rapidly becoming the baseline on new telecom satellite platforms [59]. Compared to chemical technology, this type of propulsion allows for significant improvements in the overall platform performances both in terms of mass and/or lifetime. This is achieved thanks to the increase in specific impulse of a factor between 5 and 10 which makes it possible to reduce by the same factor the propellant mass needed for station keeping throughout the life of the satellite [59]. However, since electric thrusters can only provide a very low thrust level (of the order of mN), to achieve the same station-keeping objectives that would be given for chemical propulsion it is necessary to fire the electric thrusters for long times, even hours, i.e. for a significant fraction of mission duration. Future activities are thus planned to approach the challenge of managing activations of both the electrical engine and the SAR payload at the same time, which is a required feature if electric propulsion is adopted in a NZI GEO-SAR.

ACKNOWLEDGMENT

This work has been supported by the Italian Space Agency in the framework of ASI project “Images”, contract n. 2023-32-HH.0.

REFERENCES

[1] J. C. Curlander and R. N. McDonough, *Synthetic aperture radar*, vol. 11. Wiley, New York, 1991.

[2] R. Bamler and P. Hartl, "Synthetic aperture radar interferometry," *Inverse problems*, vol. 14, no. 4, p. R1, 1998. Publisher: IOP Publishing.

[3] K. Tomiyasu, "Synthetic aperture radar in geosynchronous orbit," in *New Mexico State Univ. Proc. of the 1978 Syn. Aperture Radar Technol. Conf.*, 1978.

[4] P. A. Rosen, S. Hensley, I. R. Joughin, F. K. Li, S. N. Madsen, E. Rodriguez, and R. M. Goldstein, "Synthetic aperture radar interferometry," *Proceedings of the IEEE*, vol. 88, no. 3, pp. 333–382, 2000. Publisher: IEEE.

[5] A. Ferretti, A. Monti-Guarnieri, C. Prati, F. Rocca, and D. Massonet, *InSAR principles-guidelines for SAR interferometry processing and interpretation*, vol. 19. 2007.

[6] F. Gatelli, A. M. Guarnieri, F. Parizzi, P. Pasquali, C. Prati, and F. Rocca, "The wavenumber shift in SAR interferometry," *IEEE Transactions on Geoscience and Remote Sensing*, vol. 32, no. 4, pp. 855–865, 1994. Publisher: IEEE.

[7] C. Hu, Z. Chen, Y. Li, X. Dong, and S. Hobbs, "Research progress on geosynchronous synthetic aperture radar," *Fundamental Research*, vol. 1, no. 3, pp. 346–363, 2021. Publisher: Elsevier.

[8] A. Recchia, A. M. Guarnieri, A. Broquetas, and A. Leanza, "Impact of scene decorrelation on geosynchronous SAR data focusing," *IEEE Transactions on Geoscience and Remote Sensing*, vol. 54, no. 3, pp. 1635–1646, 2015. Publisher: IEEE.

[9] D. Bruno and S. E. Hobbs, "Radar imaging from geosynchronous orbit: Temporal decorrelation aspects," *IEEE Transactions on Geoscience and Remote Sensing*, vol. 48, no. 7, pp. 2924–2929, 2010. Publisher: IEEE.

[10] L. Cazzani, C. Colesanti, D. Leva, G. Nesti, C. Prati, F. Rocca, and D. Tarchi, "A ground-based parasitic SAR experiment," *IEEE Transactions on Geoscience and Remote Sensing*, vol. 38, no. 5, pp. 2132–2141, 2000. Publisher: IEEE.

[11] A. Monti Guarnieri and F. Rocca, "Options for continuous radar Earth observations," *Science China Information Sciences*, vol. 60, p. 060301, June 2017.

[12] T. Long, C. Hu, Z. Ding, X. Dong, W. Tian, and T. Zeng, "GEO SAR System Analysis and Design," in *Geosynchronous SAR: System and Signal Processing*, pp. 27–76, Singapore: Springer Singapore, 2018.

[13] W. N. Edelstein, S. N. Madsen, A. Moussessian, and C. Chen, "Concepts and technologies for synthetic aperture radar from MEO and geosynchronous orbits," in *Enabling Sensor and Platform Technologies for Spaceborne Remote Sensing*, vol. 5659, pp. 195–203, SPIE, 2005.

[14] J. Matar, M. Rodriguez-Cassola, G. Krieger, and A. Moreira, "On the equivalence of leo-sar constellations and complex high-orbit sar systems for the monitoring of large-scale processes," *IEEE Geoscience and Remote Sensing Letters*, vol. 21, pp. 1–5, 2024.

[15] K. Tomiyasu and J. L. Pacelli, "Synthetic aperture radar imaging from an inclined geosynchronous orbit," *IEEE transactions on geoscience and remote sensing*, no. 3, pp. 324–329, 1983. Publisher: IEEE.

[16] C. Prati, F. Rocca, D. Giancola, and A. M. Guarnieri, "Passive geosynchronous SAR system reusing backscattered digital audio broadcasting signals," *IEEE Transactions on Geoscience and Remote Sensing*, vol. 36, no. 6, pp. 1973–1976, 1998. Publisher: IEEE.

[17] L. Kou, X. Wang, M. Xiang, and M. Zhu, "Interferometric estimation of three-dimensional surface deformation using geosynchronous circular sar," *IEEE Transactions on Aerospace and Electronic Systems*, vol. 48, no. 2, pp. 1619–1635, 2012.

[18] C. Hu, Y. Li, X. Dong, R. Wang, C. Cui, and B. Zhang, "Three-dimensional deformation retrieval in geosynchronous sar by multiple-aperture interferometry processing: Theory and performance analysis," *IEEE Transactions on Geoscience and Remote Sensing*, vol. 55, no. 11, pp. 6150–6169, 2017.

[19] W. Zheng, J. Hu, W. Zhang, C. Yang, Z. Li, and J. Zhu, "Potential of geosynchronous sar interferometric measurements in estimating three-dimensional surface displacements," *Science China Information Sciences*, vol. 60, pp. 1–14, 2017.

[20] T. Long, C. Hu, Z. Ding, X. Dong, W. Tian, and T. Zeng, "Geosynchronous InSAR and D-InSAR," in *Geosynchronous SAR: System and Signal Processing*, pp. 231–272, Singapore: Springer Singapore, 2018.

[21] C. Hu, B. Zhang, X. Dong, and Y. Li, "Geosynchronous sar tomography: Theory and first experimental verification using beidou igso satellite," *IEEE Transactions on Geoscience and Remote Sensing*, vol. 57, no. 9, pp. 6591–6607, 2019.

[22] J. P. S. Stephen Hobbs, "Laplace plane and low inclination geosynchronous radar mission design," *Science China Information Sciences*, vol. 60, no. 6, 2017.

[23] J. Ruiz-Rodon, A. Broquetas, E. Makhoul, A. M. Guarnieri, and F. Rocca, "Nearly zero inclination geosynchronous SAR mission analysis with long integration time for earth observation," *IEEE Transactions on Geoscience and Remote Sensing*, vol. 52, no. 10, pp. 6379–6391, 2014. Publisher: IEEE.

[24] V. Q. de Almeida, J. Matar, M. Rodriouez–Cassola, A. Moreira, R. Haagmans, P. Bensi, and D. Petrolati, "Orbit. Performance and Observation Scenarios for Esa's Earth Explorer Mission Proposal Hydroterra," in *2021 IEEE International Geoscience and Remote Sensing Symposium IGARSS*, pp. 7740–7743, IEEE, 2021.

[25] R. Haagmans, J.-C. Calvet, G. Halloran, R. Hanssen, S. Hobbs, J. M. Lopez-Sanchez, F. Mattia, A. Monti Guarnieri, A. Moreira, and T. Nagler, "Earth Explorer 10 candidate mission Hydroterra, ESA report for assessment," 2020.

[26] G. P. Sutton and O. Biblarz, *Rocket Propulsion Elements*. Hoboken, NJ: Wiley, 9 ed., 2017.

[27] B. Thompson, T. Kelecy, T. Kubancik, T. Flora, M. Chylla, and D. Rose, "Geosynchronous patrol orbit for space situational awareness," in *Advanced Maui Optical and Space Surveillance (AMOS) Technologies Conference*, p. 96, 2017.

[28] X. Chen, Z. Chen, Y. Li, C. Hu, X. Dong, and S. Hobbs, "Improving 2D Resolution in Geosynchronous SAR via Spatial Spectrum Synthesis: Method and Verification," *IEEE Journal of Selected Topics in Applied Earth Observations and Remote Sensing*, 2024. Publisher: IEEE.

[29] "RECOMMENDATION ITU-R S.484-3* - Station-keeping in longitude of geostationary satellites in the fixed satellite service," *R S.*

[30] "RECOMMENDATION ITU-R S.743-1* - The coordination between satellite networks using slightly inclined geostationary-satellite orbits (gsos) and between such networks and satellite networks using non-inclined gso satellites," *R S.*

[31] S. Hobbs, C. Mitchell, B. Forte, R. Holley, B. Snapir, and P. Whittaker, "System design for geosynchronous synthetic aperture radar missions," *IEEE Transactions on Geoscience and Remote sensing*, vol. 52, no. 12, pp. 7750–7763, 2014.

[32] A. Monti-Guarnieri, M. Manzoni, D. Giudici, A. Recchia, and S. Tebaldini, "Vegetated target decorrelation in sar and interferometry: Models, simulation, and performance evaluation," *Remote Sensing*, vol. 12, no. 16, 2020.

[33] Y. Li, A. Monti Guarnieri, C. Hu, and F. Rocca, "Performance and requirements of geo sar systems in the presence of radio frequency interferences," *Remote Sensing*, vol. 10, no. 1, 2018.

[34] X. Dong, Y. Sui, Y. Li, Z. Chen, and C. Hu, "Modeling and analysis of rfi impacts on imaging between geosynchronous sar and low earth orbit sar," *Remote Sensing*, vol. 14, no. 13, p. 3048, 2022.

[35] S. Ceccherini, M. Massari, and A. Monti Guarnieri, "GEOSAR: orbits and flying formation," May 2019.

[36] J. Nicolás-Álvarez, X. Carreño-Megias, E. Ferrer, M. Albert-Galí, J. Rodríguez-Tersa, A. Aguasca, and A. Broquetas, "Interferometric orbit determination system for geosynchronous SAR missions: Experimental proof of concept," *Remote Sensing*, vol. 14, no. 19, p. 4871, 2022. Publisher: MDPI.

[37] A. Moussessian, C. Chen, W. Edelstein, S. Madsen, and P. Rosen, *System Concepts and Technologies for High Orbit SAR (Invited)*. July 2005.

[38] J. Matar, M. Rodriguez-Cassola, G. Krieger, and A. Moreira, "On the equivalence of leo-sar constellations and complex high-orbit sar systems for the monitoring of large-scale processes," *IEEE Geoscience and Remote Sensing Letters*, vol. 21, pp. 1–5, 2024.

[39] J. Matar, M. Rodriguez-Cassola, E. R. Silva Filho, N. Sakar, V. Gracheva, M. Suess, G. Krieger, and A. Moreira, "A LEO-SAR Constellation Equivalent to an Interferometric Geosynchronous Mission," in *IGARSS 2023-2023 IEEE International Geoscience and Remote Sensing Symposium*, pp. 4706–4709, IEEE, 2023.

[40] C. Hu, T. Long, Z. Liu, T. Zeng, and Y. Tian, "An improved frequency domain focusing method in geosynchronous SAR," *IEEE Transactions on Geoscience and Remote Sensing*, vol. 52, no. 9, pp. 5514–5528, 2013. Publisher: IEEE.

[41] C. Prati, F. Rocca, D. Giancola, and A. Guarnieri, "Passive geosynchronous sar system reusing backscattered digital audio broadcasting signals," *IEEE Transactions on Geoscience and Remote Sensing*, vol. 36, no. 6, pp. 1973–1976, 1998.

[42] A. M. Guarnieri, O. Bombaci, C. Germani, G. Orlando, D. Giudici, D. Schulz, and V. T. Khang, "Quasi geostationary, comsat-compatible SAR: Solutions for payload design," in *2015 IEEE International Geo-*

science and Remote Sensing Symposium (IGARSS), pp. 4590–4593, IEEE, 2015.
[43] A. M. Guarnieri, A. Broquetas, A. Recchia, F. Rocca, and J. Ruiz-Rodon, "Advanced radar geosynchronous observation system: ARGOS," *IEEE Geoscience and Remote Sensing Letters*, vol. 12, no. 7, pp. 1406–1410, 2015. Publisher: IEEE.
[44] Y. Li, A. Monti Guarnieri, C. Hu, and F. Rocca, "Performance and requirements of GEO SAR systems in the presence of radio frequency interferences," *Remote Sensing*, vol. 10, no. 1, p. 82, 2018. Publisher: MDPI.
[45] A. Monti Guarnieri, A. Leanza, A. Recchia, S. Tebaldini, and G. Venuti, "Atmospheric phase screen in geo-sar: Estimation and compensation," *IEEE Transactions on Geoscience and Remote Sensing*, vol. 56, no. 3, pp. 1668–1679, 2018.
[46] A. Monti-Guarnieri, M. Manzoni, D. Giudici, A. Recchia, and S. Tebaldini, "Vegetated target decorrelation in sar and interferometry: Models, simulation, and performance evaluation," *Remote Sensing*, vol. 12, no. 16, 2020.
[47] F. Ulaby, M. C. Dobson, and J. L. Álvarez-Pérez, *Handbook of radar scattering statistics for terrain*. Artech House, 2019.
[48] A. Aguasca, A. Broquetas, J. M. Lopez-Sanchez, X. Fàbregas, J. J. Mallorqui Franquet, and M. Mas, "Assessment of the impact of long integration time in geosynchronous sar imagery of agricultural fields by means of gb-sar data," *IEEE Journal of Selected Topics in Applied Earth Observations and Remote Sensing*, vol. 17, pp. 1338–1347, 2024.
[49] J. Kellndorfer, O. Cartus, M. Lavalle, C. Magnard, P. Milillo, S. Oveisgharan, B. Osmanoglu, P. A. Rosen, and U. Wegmüller, "Global seasonal sentinel-1 interferometric coherence and backscatter data set," *Scientific Data*, vol. 9, no. 1, p. 73, 2022.
[50] F. Rocca, "Diameters of the orbital tubes in long-term interferometric SAR surveys," *IEEE Geoscience and Remote Sensing Letters*, vol. 1, no. 3, pp. 224–227, 2004.
[51] G. Sentinel, "Team, GMES Sentinel-1 System Requirements Document," tech. rep., Technical Report S1-RS-ESA-SY-0001, ESA, 2006.
[52] A. Weiss, U. V. Kalabić, and S. D. Cairano, "Station keeping and momentum management of low-thrust satellites using mpc," *Aerospace Science and Technology*, vol. 76, pp. 229–241, 2018.
[53] H. Li, *Geostationary Satellites Collocation*. Springer, 2014.
[54] D. A. Vallado, *Fundamentals of astrodynamics and applications*, vol. 12. Springer Science & Business Media, 2001.
[55] B. Thompson, T. Kelecy, T. Kubancik, T. Flora, M. Chylla, and D. Rose, "Geosynchronous patrol orbit for space situational awareness." [Online], 2017. Accessed: Nov. 19, 2023.
[56] G. Zhang, H. Zhang, and X. Cao, "New solutions to impulsive correction for argument of perigee using gauss's variational equations," *Journal of Aerospace Engineering*, vol. 32, no. 5, 2019.
[57] H. D. Curtis, *Orbital Mechanics for Engineering Students*. Butterworth-Heinemann, third edition ed., 2014.
[58] NASA, "General mission analysis tool (gmat)," 2019. Accessed: December 27, 2024.
[59] D. Losa, *High vs Low Thrust Station Keeping Maneuver Planning for Geostationary Satellites*. PhD thesis, École Nationale Supérieure des Mines de Paris, 2007.
[60] W. Torge, *Geodesy*. Berlin, Germany: De Gruyter, 4th ed., 2012.
[61] V. N. Dvornychenko, "The generalized tsiolkovsky equation," in *NASA, Goddard Space Flight Center, Flight Mechanics (Estimation Theory Symposium)*, (Anaheim, CA, United States), NASA, December 1 1990. Work of the US Gov. Public Use Permitted.
[62] G. R. Schmidt, M. J. Patterson, and S. W. Benson, "The nasa evolutionary xenon thruster (next): The next step for u.s. deep space propulsion," in *Proceedings of the International Astronautical Congress (IAC)*, vol. IAC-08-C4.4.2, NASA Glenn Research Center, 2008.
[63] J. Nicolás-Álvarez, X. Carreño-Megias, E. Ferrer, M. Albert-Galí, J. Rodríguez-Tersa, A. Aguasca, and A. Broquetas, "Interferometric orbit determination system for geosynchronous sar missions: Experimental proof of concept," *Remote Sensing*, vol. 14, p. 4871, 2022.